Cone-Opponent Ganglion Cells in the Primate Fovea Tuned to Non-Cardinal Color Directions

Tyler Godat[1,2], Kendall Kohout[1], Qiang Yang[1], Keith Parkins[1], Juliette E. McGregor[1,3], William H. Merigan[1,3], David R. Williams[1,2,3], Sara S. Patterson[1,*]

[1] Center for Visual Science, University of Rochester, Rochester, NY, 14607

[2] Institute of Optics, University of Rochester, Rochester, NY, 14627

[3] Flaum Eye Institute, University of Rochester Medical Center, Rochester, NY, 14642

∗ Correspondence: spatte16@ur.rochester.edu

A long-standing question in vision science is how the three cone photoreceptor types – long (L), medium (M) and short (S) wavelength sensitive – combine to generate our perception of color. Hue perception can be described along two opponent axes: red-green and blue-yellow. Psychophysical measurements of color appearance indicate that the cone inputs to the red-green and blue-yellow opponent axes are M vs. L+S and L vs. M+S, respectively. However, the "cardinal directions of color space" revealed by psychophysical measurements of color detection thresholds are L vs. M and S vs. L+M. The cardinal directions match the most common cone-opponent retinal ganglion cells (RGCs) in the primate retina. Accordingly, the cone opponency necessary for color appearance is thought to be established in cortex. However, small populations with the appropriate M vs. L+S and L vs. M+S cone-opponency have been reported in large surveys of cone inputs to primate RGCs and their projections to the lateral geniculate nucleus (LGN) yet their existence continues to be debated. Resolving this long-standing open question is needed as a complete account of the cone-opponency in the retinal output is critical for efforts to understand how downstream neural circuits process color. Here, we performed adaptive optics calcium imaging to longitudinally and noninvasively measurements of the foveal RGC light responses in the living macaque eye. We confirm the presence of L vs. M+S and M vs. L+S neurons with non-cardinal cone-opponency and demonstrate that cone-opponent signals in the retinal output are substantially more diverse than classically thought.

INTRODUCTION

A goal of visual neuroscience is to determine how information is organized and represented at various stages of the visual system to give rise to our perception of the world. To understand color perception, a fundamental line of investigation focuses on determining how the outputs of the L-, M- and S-cones at each stage of the visual system. These questions are especially critical at "information bottlenecks" like the optic nerve; retinal ganglion cells (RGCs) provide the sole source of visual input to the cortex and thus make up the building blocks for all vision-related computations. As such, a full account of cone opponency in the retinal output is essential for developing a comprehensive understanding of the cortical processing contributing to color perception.

In the primate early visual system, the cones are combined into three axes often referred to as the "cardinal directions of color space". One direction is responsive to changes in luminance (L+M), while the other two respond to isoluminant chromatic modulations (L vs. M and S vs. L+M). The cardinal directions of were established in a highly influential study measuring changes in detection thresholds after chromatic contrast adaptation (Krauskopf et al., 1982). A follow-up physiological survey in the LGN revealed that most neurons are tuned to these axes (Derrington et al., 1984) and consolidated the theoretical basis for the widely used DKL color space in **Fig. 1A** (Brainard, 1996). In the retina, the cone inputs to the cardinal directions match the three most common RGC types, the parasol, midget and small bistratified (Calkins, 2000). Based on these compelling lines of evidence, the cardinal axes have served as the basis for most color vision models (Lennie and D'Zmura, 1988; De Valois and De Valois, 1993; Stockman and Brainard, 2010).

Despite this consensus between retinal cone opponency and the impact of contrast adaptation on color detection, the cardinal directions and their underlying cone-opponent neurons do not account for some key aspects of human color vision. L vs. M and S vs. L+M does not match the cone opponency derived from psychophysical

measurements of red-green and blue-yellow color appearance: L vs. M+S and M vs. L+S, respectively (Werner and Wooten, 1979; Webster et al., 2000a; De Valois, 2004a; Shevell and Martin, 2017). As shown in **Fig. 1A**, stimulus modulations along the cardinal chromatic directions, which are often referred to as "red-green" and "blue-yellow" (Stromeyer et al., 1998; Conway, 2001; Vogelstein et al., 2010), are instead perceived as magenta-cyan and lavender-lime. While L - M may appear close to red in the isoluminant plane of DKL color space, plotting the data along a wavelength axis in **Fig. 1B** demonstrates a substantial disagreement: red, for example, is perceived at both ends of the spectrum (Ingling, 1977; Fuld et al., 1981).

The dominant hypotheses propose cortical processing resolves the ambiguities between retinal cone opponency, color detection and color appearance (De Valois and De Valois, 1993; Li et al., 2022). In these theoretical "multi-stage" models (**Fig. 1C**), the cones are the first stage, and the retinal computations that establish L vs. M and S vs. L+M cone opponency the second stage. A third stage combines the outputs of the L vs. M opponency and S-cone input.

An alternative hypothesis prompted by the confounded spectral and spatial information in L vs. M midget RGCs proposes that L vs. M neurons mediate achromatic spatial vision while other RGCs with the cone opponency predicted by color appearance psychophysics contribute to hue (Rodieck, 1991; Calkins and Sterling, 1999; Schmidt et al., 2014; Neitz and Neitz, 2017). In these models, a greater diversity of computations at the second stage replaces the need for the third stage in **Fig. 1C**. While some studies have identified small populations of neurons with the appropriate L vs. M+S and M vs. L+S cone opponency (De Monasterio and Gouras, 1975; Padmos and Norren, 1975; De Monasterio, 1978; Derrington et al., 1984; Tailby et al., 2008b), others have not (Chatterjee and Callaway, 2003; Sun et al., 2006); thus, their existence remains highly controversial.

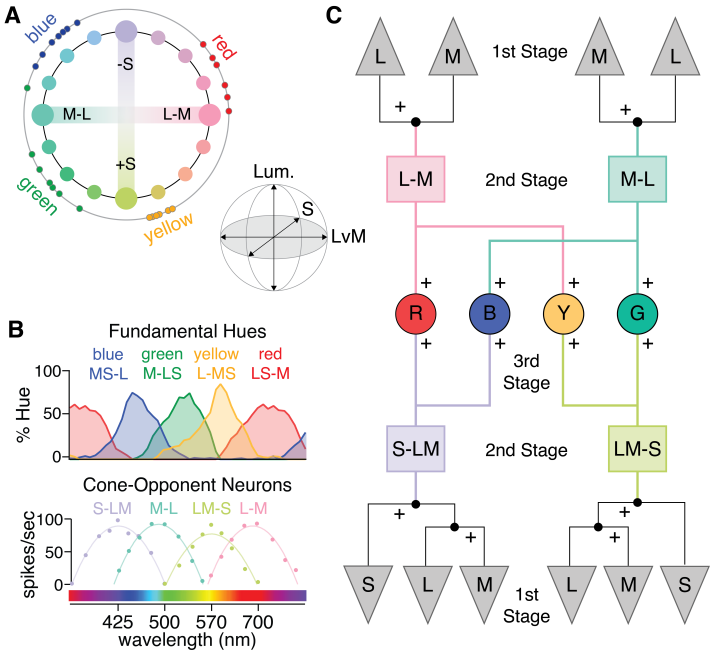

Figure 1. The most common cone-opponent neurons in the primate early visual system do not match hue perception. (A) The inner circle shows the isoluminant plane of DKL color space (inset; gray shading), formed by the cardinal L vs. M and S axes. The outer circle shows the locations of the four unique hues for multiple participants (Webster et al., 2000b; Shevell and Martin, 2017). The unique hues are not located on the cardinal L vs. M and S axes and thus require a combination of L vs. M and S-cone input. **(B)** The responses of L vs. M and S vs. L+M neurons (bottom) do not align with the fundamental hues (top). Adapted from hue scaling and LGN neuron physiology (De Valois, 2004b). **(C)** A standard three-stage color vision model. The cardinal directions reflect the second stage consistent with color detection. Downstream mixing of their outputs forms a third stage with cone opponency that can explain color appearance (adapted from Stockman & Brainard, 2010).

The difficulty in confirming or denying the existence of RGCs tuned to non-cardinal color directions stems from two technical challenges facing standard retinal physiology techniques. First, the fovea plays a major role in color perception, yet its fragility has largely limited direct investigation of the underlying retinal physiology to the periphery. Second, rarer primate RGC types are difficult to systematically investigate in acute experiments and many anatomically-identified types have yet to be characterized functionally. To overcome these challenges, we used adaptive optics calcium imaging ophthalmoscopy to non-invasively and repeatedly image the responses of hundreds of individual foveal RGCs in the living macaque eye.

METHODS

Animal Care. Three macaques (*Macaca fascicularis*) were housed in pairs in an AAALAC accredited facility. All animals were in the care of the Department of Comparative Medicine veterinary staff of the University of Rochester's Medical Center, including several full-time veterinarians, veterinary technicians, and an animal care staff who monitored animal health. Additional details on the vivarium environment are detailed in our prior work (McGregor et al., 2020; Godat et al., 2022). This study was carried out in strict accordance with the Association

for Research in Vision and Ophthalmology (ARVO) Statement for the Use of Animals and the recommendations in the Guide for the Care and Use of Laboratory Animals from the National Institutes of Health. The animal protocol was approved by the University Committee on Animal Resources (UCAR) of the University of Rochester under PHS assurance number D16-00188 (A3292-01).

Viral Delivery. All three macaques (M2, M3 and M4) received subcutaneous Cyclosporine A prior to injection of viral vectors. Blood trough levels were collected weekly to titrate the dosage into the range of 150–200 ng ml-1 and then maintained at that level. M2 began immune suppression in March 2018 with 6 mg kg-1, which was stepped down to 4 mg kg-1 a month later. M3 started immune suppression in May 2019 at 6 mg kg-1, which was stepped down a month later to 3.4 mg kg-1. M4 began immune suppression in December 2020 at 4 mg kg-1 and maintained this level.

The intravitreal injections used in this study have been described in full previously (Yin et al., 2011) and are summarized below. The vector AAV2-CAG-GCaMP6s was synthesized by the Pennsylvania Vector Core. Injections were made into both eyes of each animal. Prior to injection, eyes were sterilized with 50% diluted Betadine, and the injection was made in the middle of the vitreous approximately 4 mm behind the limbus using a tuberculin syringe and 30-gauge needle. Following injection, each eye was imaged with a conventional scanning light ophthalmoscope (Heidelberg Spectralis) using the 488 nm autofluorescence modality to determine onset of GCaMP expression in the ganglion cell layer (GCL) and to monitor eye health. The data in this study was collected 1-year post-injection for M2, 1.3 years post-injection for M3 and 1.4 years post-injection for M4.

Imaging Preparation. Anesthesia and animal preparation procedures have been previously published (McGregor et al., 2020; Godat et al., 2022) and are briefly summarized here. All anesthesia and preparation followed established lab protocols and was performed by a veterinary technician licensed by the State of New York (USA). All animals were fasted overnight prior to anesthesia induction the morning of an imaging session. During a session, animals were placed prone onto a custom stereotaxic cart and covered with a Bair Hugger warming system to maintain body temperature. Monitoring devices including rectal temperature probe, blood pressure cuff, electrocardiogram leads, capnograph, and a pulse oximeter, were used to track and record vital signs. Temperature, heart rate and rhythm, respirations and end tidal CO2, blood pressure, SPO2, and reflexes were monitored and recorded every fifteen minutes. Pupil dilation was accomplished using a combination of 1% Tropicamide and 2.5% Phenylephrine. A full list of all medications used and a full description of the anesthesia, intubation, pupil dilation, and recovery processes can be found in our previous work (McGregor et al., 2020).

Adaptive Optics Scanning Laser Ophthalmology. Data were collected using an adaptive optics scanning light ophthalmoscope (AOSLO) previously described (Gray et al., 2006; Godat et al., 2022). Briefly, an 847 nm diode laser (QPhotonics) was used as a wavefront sensing beacon with a Shack-Hartmann wavefront sensor to measure animals' wavefront aberrations in real time (20 Hz sample rate). A deformable mirror (ALPAO) with 97 actuators was used to correct the measured aberrations in closed loop at approximately 8 Hz across a 7.2 mm diameter pupil. A 796 nm center wavelength superluminescent diode (Superlum) was focused on the foveal cone photoreceptor mosaic to collect images (using an 2 Airy disk confocal image, 20 µm) used for navigating to the same retinal location in each experiment and for offline motion correction/registration of fluorescence images. Three LEDs (ThorLabs; center wavelengths and full-widths-at-half-maximum of 420 ± 7 nm, 530 ± 17 nm, 660 ± 10 nm) were presented to the foveal cones via a Maxwellian view stimulator (Westheimer, 1966; Baron, 1973). A 488 nm laser (Qioptiq) was focused on the GCL and used to excite fluorescence from GCaMP6-expressing cells, which was detected through a 520/35 nm filter (using a 2 Airy disk confocal pinhole, 20 µm in M2/M3, 25 µm in M4). The 488 nm excitation laser was presented only during forward raster scans of the AOSLO and filled only the portion of the imaging field where RGCs were present (i.e., laterally displaced from the foveal cones and axially displaced to focus on the GCL). The constant adapting light presented with the LEDs has been demonstrated to mitigate responses to the spatially offset imaging light (Godat et al., 2022). Room lights were turned off during experiments to minimize ambient light.

All light sources were delivered through a dilated pupil of approximately 6.7 mm. The 488 nm excitation laser intensities on the retina were 3.2 mW cm-2 in M2, 1.7 mW cm-2 in M3, and 1.4 mW cm-2 in M4. Imaging fields of view subtended approximately 765 x 560 µm in M2, 740 x 540 µm in M3, and 740 x 540 µm in M4. The total

retinal exposure to all light sources was calculated prior to each imaging session – source powers measured at the animal's pupil were nominally 7-15 µW at 488 nm, 250 µW at 796 nm, 30 µW at 847 nm and 5 µW from the three LEDs. The total exposure during an experiment was kept below the maximum permissible exposure for human retina according to the 2014 American National Standards Institute and most exposures were also below a reduced limit that was further scaled by the squared ratio of the numerical aperture of the human eye to the primate eye (∼0.78-0.85). In this study, exposures during 2-4 hours of imaging ranged from 60-94% of the human retinal limit, with the majority between 60-85%. All sessions were spaced a minimum of 5 days apart per animal, so cumulative light exposure was not calculated.

Each animal had no known history of ocular disease or vision abnormality. Each animal was fitted with a custom contact lens to enhance wavefront correction. The nasal retina of the left eye was imaged for M2 and temporal retina of the right eye was imaged for M3 and M4. The imaged eye of M2 had an axial length of 17.2 mm and dioptric power 57.5 D x 45° and 56.7 D x 135°. M3's imaged eye had an axial length of 16.6 mm and dioptric power of 61.1 D x 85° and 61.8 D x 175°. M4's imaged eye had an axial length of 16.9 mm and dioptric power of 60.1 D x 5° and 66.6 D x 95°.

Data Analysis. Fluorescence videos were co-registered with the simultaneously-acquired reflectance videos (**Fig. 2**) frame-by-frame with a strip-based cross-correlation algorithm (Yang et al., 2014). Registration was performed relative to a reference image of the cone mosaic, taken during the experiment and used for online stabilization. For each experiment, a registered fluorescence video from the control trial was summed across frames to create an image of the GCL for region of interest (ROI) segmentation using GIMP (RRID: SCR_003182). Unless otherwise stated, analyses below were performed in MATLAB (Mathworks, RRID: SCR_001622). Final figures were created in Igor Pro 9 (Wavemetrics, RRID: SCR_000325) and Illustrator (Adobe, RRID: SCR_010279).

Visual Stimuli. Once a fit was calculated, the original segmentation mask of the target cell was applied to the modeled fit, and the overlap percentage was calculated as the sum of pixel intensities from nearest neighbors within the segmentation divided by the total sum of pixel intensities within the ROI (**Fig. 4B-D**). This value, expressed as a percentage, gives an upper bound on how much light could have fallen within the ROI that originated from neighboring cells. This value represents an upper bound because cells have definite sharp borders, and despite a modest amount of optical blur and scattered light, their light distributions lack the spatial extent described by a Gaussian function. Thus, the overlap metric is a conservative estimate of potential optical crosstalk.

To analyze each sinusoidal stimulus, each ROI's responses (average of three presentations per stimulus) were filtered using a Hann windowing function and then Fourier transformed using custom software (Frequency Analysis, available at `https://osf.io/s9qw4`). The phase and amplitude at the modulation frequency were used to quantify the strength and sign of the response to each stimulus. The phase was used to classify responses as ON or OFF-dominant. Fourier amplitudes at the stimulus frequency were normalized for each cell by subtracting the mean noise of higher frequencies (0.32 – 1.08 Hz) and then dividing the standard deviation (SD) of the noise to produce a response metric equivalent to the sensitivity index d-prime (d'). A cutoff of two SDs (dashed lines in **Fig. 3**) was chosen for significance which produced a 2.7% false positive rate across all ROIs in each experiment (i.e., 2.7% of all ROIs exceeded 2 SDs for the control stimulus). When each ROI's responses were averaged across experiments, only 1 of the 486 cells imaged exceeded this cutoff for the control stimulus.

Between experiments there are slight changes of axial focus which can impact the measured strength of an ROI's stimulus-driven response. However, these small focus changes could also increase and decrease the contributions of out-of-focus cells as well. Rather than try to distinguish between these alternatives, we chose to omit all cells without significant responses in at least two experiments (of two for M2/M3 and three for M4). This constraint likely leads to false rejections but increases confidence in those cells which did respond significantly and reliably across experiments

Sum of Gaussians Model and Crosstalk Analysis. To calculate the upper bound for overlapping light distributions contributing responses to a single segmented ROI, we developed a sum of Gaussians model. This model allowed quantification of the possibility that cells with non-cardinal cone opponency reflect the responses from two more common cone-opponent neurons, one with S-cone responses and one with L vs. M cone opponency. For each target cell, a new mask was manually placed centered on the target cell and including the nearest 8–14

neighboring cells (many of which were not initially segmented due to evidence for poor optical isolation in at least one experiment). This mask was applied to the fluorescence image to restrict fitting to the neighborhood around each target cell.

To fit the target cell and its nearest neighbors in each fluorescence image, a sum of two-dimensional Gaussians of the following form was used:

$$G(x,y) = b + \sum_{n=1}^{N} A_n * e^{(-\frac{(x-x_n)^2}{2\sigma_n^2} - \frac{(y-y_n)^2}{2\sigma_n^2})} \tag{1}$$

where b is the minimum background pixel value within the mask, N is the number of ROIs in the image, A_n is the Gaussian amplitude for the n-th cell, (x_n, y_n) is the center coordinates of the n-th Gaussian, and a_n is the standard deviation of the n-th Gaussian. A nonlinear least-squares fit was used to match the sum of Gaussians model to the measured data. For the fit, (x_n, y_n) were fixed while A_n and a_n were free parameters. This method was chosen because the center of each cell was clearly identifiable and allowing (x_n, y_n) to vary freely would have required an arbitrarily high number of Gaussians for a given image. Contrast stretching was employed during cell identification to ensure all cells were identified and assigned x and y values. A lower bound of unity was set for both A_n and a_n. The images ranged from 0-255, so a Gaussian could not have $A_n < 1$ and $a_n < 1$ (soma size less than ∼1.5 µm) is inconsistent with published reports of foveal RGC somas (Curcio and Allen, 1990). Pixels outside the mask, but within the mask's bounding box were set to the minimum value within the mask (b) to assist with fitting (**Fig. 4A**).

Once a fit was calculated, the original segmentation mask of the target cell was applied to the modeled fit, and the overlap percentage was calculated as the sum of pixel intensities from nearest neighbors within the segmentation divided by the total sum of pixel intensities within the ROI (**Fig. 4B-D**). This value, expressed as a percentage, gives an upper bound on how much light could have fallen within the ROI that originated from neighboring cells. This value represents an upper bound because cells have definite sharp borders, and despite a modest amount of optical blur and scattered light, their light distributions lack the spatial extent described by a Gaussian function. Thus, the overlap metric is a conservative estimate of potential optical crosstalk.

To interpret the upper bounds of overlap for each L vs. M ± S cell, we compared the overlap to the modulation depth for each stimulus (**Fig. 4E**). The Fourier amplitude at the frequency stimulation and the DC offset (Fourier amplitude at the zero frequency) were obtained from the one-sided power spectrum and used to compute the modulation depth (M_S) for each stimulus (s) in the following way:

$$M_s = 100 * \frac{A_n}{A_n^0} * \frac{1}{C_s} \tag{2}$$

where A_n is the Fourier amplitude of the n-th cell at the modulation frequency, A_n^0 is the DC offset of the n-th cell, and C_s is the cone modulation of stimulus s. In M2, C_{L-M} was 0.153 and C_S was 0.688. In M3, C_L was 0.243, C_M was 0.325 and C_S was 0.92. In M4, C_L was 0.258, C_M was 0.354 and C_S was 0.939.

The maximum modulation explainable by optical crosstalk for each L vs. M ± S cell is the product of the percent overlap and the maximum modulation across all segmented neurons (dashed line in **Fig. 4E**). If the cell's lowest modulation depth exceeded this value, then their responses could not be explained by optical crosstalk from neighboring cells.

RESULTS

Longitudinal imaging of foveal ganglion cell physiology in the living macaque eye

We leveraged a powerful *in vivo* retinal physiology technique that combines adaptive optics scanning laser ophthalmoscopy with calcium imaging to present visual stimuli and image RGC responses at the center of the living macaque fovea (Gray et al., 2006; McGregor et al., 2018). GCaMP6s expression in the foveal ganglion cell layer was obtained through intravitreal injections of *AAV2:CAG:GCaMP6s* (Yin et al., 2011; Chen et al., 2013). The ubiquitous promoter CAG is not RGC-specific; however, displaced amacrine cells make up just 1-2% of the foveal ganglion cell layer and no amacrine cell has been identified with L vs. M cone opponency (Curcio and Allen, 1990; Calkins and Sterling, 1996).

The imaging paradigm is depicted in **Fig. 2** and described in full in the **Methods**. Briefly, the cellular resolution necessary to non-invasively image calcium responses *in vivo* was achieved with adaptive optics, which detects and corrects for the eye's monochromatic aberrations in real time (Liang and Williams, 1997; Williams et al., 2023. Reflectance imaging of the cone mosaic was used for online eye tracking, offline registration and to navigate to the same retinal location across imaging sessions. Fluorescence imaging of the foveal RGCs was performed while visual stimuli were presented to the cones with a Maxwellian view stimulator. Due to the natural spatial displacement of foveal RGCs from their cone inputs, the imaging light was displaced both laterally and axially from the RGCs' cone inputs and the visual stimuli.

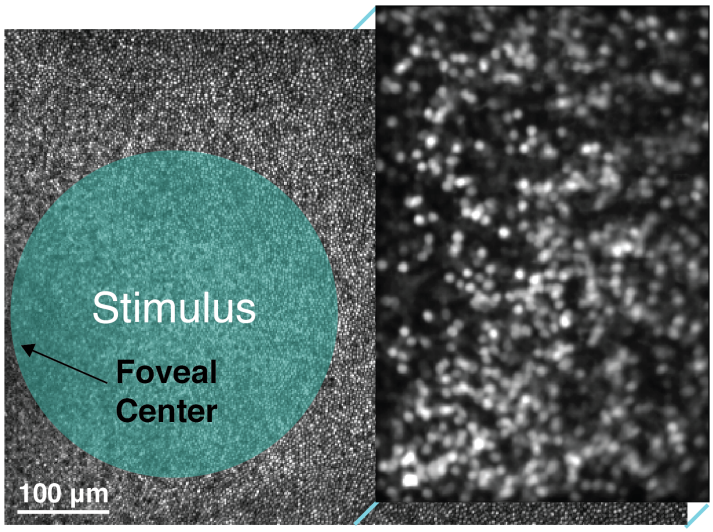

Figure 2. Experimental paradigm for stimulus delivery and calcium imaging in the living macaque fovea. Diagram illustrating the *in vivo* calcium imaging paradigm with adaptive optics scanning laser ophthalmoscopy. Data from M4 is shown with a 3.69 x 2.70º field of view. Reflectance imaging (796 nm) of the cone mosaic was performed across the full field of view while fluorescence imaging (488 nm) was restricted to the right half of the field of view and focused on GCaMP6s-expressing RGCs in the ganglion cell layer. Visual stimuli were focused on the foveal cones on the left. A wavefront sensing channel (847 nm) for real-time detection and correction of the eye's aberrations with adaptive optics is not pictured.

The unique advantages of this approach are well-suited to resolving the question of whether neurons tuned to non-cardinal color directions are present in the primate retina. Despite the fovea's key role in color perception, its fragility poses a major obstacle for ex vivo electrophysiology techniques. As a result, our understanding of foveal cone-opponent RGCs is largely inferred from anatomy and their response properties in the retinal periphery, despite evidence that foveal neurons differ from their peripheral counterparts in unexpected ways (Sinha et al., 2017; Lee et al., 2018; Baudin et al., 2019). With our non-invasive calcium imaging approach, we were able to study foveal RGCs in their natural habitat (the living eye). Simultaneously recording from hundreds of foveal RGCs increased the likelihood of finding rarer cone-opponent RGC types. Moreover, we can return to the same RGCs in subsequent sessions to demonstrate the reliability of our measurements and study the rarer types in detail. These advantages enabled us to provide new insight into the classic question of cone-opponency in the primate retinal output.

During a larger study on spatial frequency tuning of L vs. M foveal midget RGCs, we identified candidate L vs. M+S and M vs. L+S neurons with cone-isolating, isoluminant and achromatic stimuli modulated sinusoidally in time (Godat et al., 2022). Here, we performed a focused investigation of these neurons, incorporating new data (**Fig. 3A**), comprehensive analyses of the neurons with unexpected cone opponency (**Fig. 3B**), and a qualitative model for validating their optical isolation (**Fig. 4**). In total, we analyzed 486 well-isolated neurons across three macaques (M2, M3 and M4). The somas of the foveal RGCs imaged lay at the margins of the foveal pit, approximately 1-4° from the foveal center. Using a previously published modeling approach (McGregor et al., 2018), these RGCs are likely to be driven by cones within 36 arcmin eccentricity (within 120 µm radius from the foveal center). 83.74% (407/486) of these neurons responded significantly to at least one stimulus when averaged across experiments. 78.2% (380/486) responded reliably between experiments, which were separated by a week or more. The 106 neurons that either did not respond significantly to any stimulus or exhibited unreliable responses to one or more stimuli were omitted from all subsequent analyses.

Cone opponency in the primate fovea

We classified the cone inputs to the 380 reliably responsive retinal neurons and plotted the results along the cardinal axes (**Fig. 3A**). For the 274 neurons from M3 and M4, L- and M-cone isolating stimuli were used instead of an L vs. M isoluminant stimulus, which enabled identification of cells with either L- or M-cone input. These neurons could not be accurately plotted along the L vs. M axis of **Fig. 3A** and are instead plotted separately on an L- vs. M-cone axis (**Fig. 3B**).

L vs. M neurons were the dominant cone-opponent population in our dataset, making up 43.68% (166/380). In

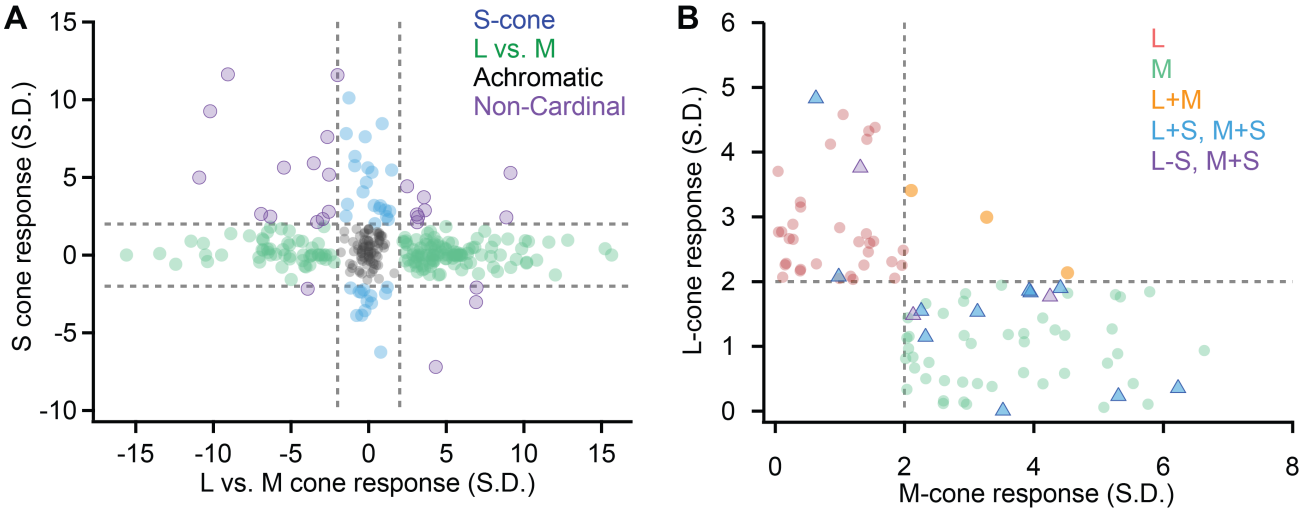

Figure 3. Functional classification of cone opponency in the living primate fovea. (A) Cone opponency of foveal cells from three macaques along the cardinal chromatic axes (L vs. M and S), classified based on their response at the stimulus frequency in units of standard deviations above noise (d-prime). Dashed lines indicate the "responsivity" threshold of two standard deviations. **(B)** Neurons with either L- or M-cone input as determined by the L- and M-cone isolating stimuli used in M3 and M4 (274 neurons total). Note that the M-cone isolating stimulus had 1.3x higher contrast than the L-cone isolating stimulus. The subset of S-ON and S-OFF neurons with either L- or M-cone input are replotted from 3A, the remainder could not be accurately plotted in the L vs. M and S cone-opponent space.

the 274 neurons tested with L- and M-cone isolating stimuli, 30 responded to L-cone isolating stimulus only and 40 to M-cone isolating stimulus only (**Fig. 3B**). Interestingly, only 3 neurons had significant responses to both the L- and M-cone isolating stimulus that were in phase (L+M). The largest population of L+M neurons, parasol RGCs, are thought to make up 6% of the foveal output (Ma et al., 2023). This discrepancy is likely due to stimulus choice. To accommodate population-level data collection and Fourier analysis with a slow calcium indicator, we used a large spatially-uniform stimulus (1.3° diameter) and low temporal frequencies (0.15-0.2 Hz). Together, these features made our stimulus ineffective for neurons with transient responses and/or strong surround receptive fields, which are common features of parasol RGCs and other magnocellular LGN-projecting RGCs (Derrington and Lennie, 1984).

Nonetheless, 21.6% of the neurons had significant responses only to the achromatic stimulus. While these neurons could include parasol RGCs, their high density suggests many are instead midget RGCs. In the fovea, the center-surround receptive fields of L vs. M midget RGCs compare the photon catch in the single L- or M-cone center to the photon catch in neighboring L/M-cones in the surround. As the relative numbers of L- and M-cones in the midget RGCs' surround receptive field are largely random (Lennie et al., 1991; Buzás et al., 2006; Field et al., 2010), L-cone center midget RGCs, for example, can vary from strongly cone-opponent (only M-cones in the surround) to achromatic (only L-cones in the surround). As a result, many midget RGCs may respond well to the high contrast achromatic stimulus, but lack sufficient L vs. M opponency to generate significant responses.

Another 6.6% (25/380) of cells did not fall along the cardinal axes because they exhibited both L vs. M opponency and S-cone input: 8 (L+S)-M, 3 L-(M+S), 13 (M+S)-L and 1 M-(L+S). These neurons likely correspond to the "red-cyan" and "green-magenta" neurons reported in prior surveys of cone-opponency in the macaque early visual system (De Monasterio et al., 1975; Conway, 2001). Because their role in vision remains unclear, we refer to the four groups collectively as L vs. M±S neurons. The cone-opponent combinations to these four groups are consistent with the cone inputs to the four fundamental hues: red, green, blue, and yellow (**Fig. 1**). In M3 and M4, the use of L- and M-cone isolating stimuli instead of an isoluminant stimulus enabled identification of cells with either L- or M-cone input and revealed three neurons with non-cardinal cone opponency: 2 –(M+S) and 1 L+S (**Fig. 3B**). These neurons are distinct from the well-studied S vs. L+M cells in that the S-cone response is in phase with L or M. Given the stringent responsivity cutoff employed in our classification along with the low contrast and temporal frequency of the L- and M-cone isolating stimuli (see **Methods**), it is possible these neurons have weak responses from the missing L- or M-cone that eluded detection. Including the M+S and L+S neurons, the total number of neurons tuned to non-cardinal color directions was 7.4% (28/380).

We also identified a smaller population of neurons falling along the S-cone axis (5.3% S-ON and 2.4% S-OFF). The density of S-ON neurons is slightly higher than expected as small bistratified RGCs are estimated at 2-3% of foveal RGCs (Dacey, 1993). This discrepancy could reflect the inclusion of rarer S-ON neurons, such as large bistratified RGC, ON narrow thorny RGC, M2 intrinsically photosensitive RGCs and displaced S-cone amacrine cell (Dacey and Packer, 2003; Patterson et al., 2020b, 2020a; Mazzaferri et al., 2023), or the location of the imaging plane within the foveal ganglion cell later (discussed below). It is worth noting that many of the S-ON and S-OFF neurons did not have significant responses to both the L- and M-cone isolating stimulus. We observed 9 neurons with M vs. S responses (6 S-ON/M-OFF and 3 M-ON/S-OFF) and 2 neurons with L vs. S responses (both L-ON/S-OFF), with responses to the missing L- or M-cone likely falling below our responsivity threshold (**Fig. 3B**). The larger number of M vs. S neurons is likely due to the higher contrast of the M-cone isolating stimulus (see **Methods**). These L vs. S and M vs. S neurons could be either S vs. (L+M) neurons like the small bistratified and S-OFF midget RGC, or (S+L)-M/(S+M)-L. Because these two groups could not be distinguished, the L vs. S and M vs. S neurons were classified as S-ON and S-OFF neurons.

Taken together, these results confirm the presence of L vs. M+S and M vs. L+S neurons in the primate fovea. Because they have both S-cone input and L vs. M cone-opponency, these neurons are not located along the cardinal color directions and are categorically distinct from the well-studied S vs. L+M and L vs. M RGCs. However, two caveats limit our ability to provide a precise estimate of the true density of neurons tuned to non-cardinal color directions. First, the location of the responsivity cutoff (gray dashed lines in **Fig. 3**) defined the final classification of cone-opponent neurons. We chose a highly stringent criterion to maximize confidence in identified cone-opponent neurons rather than detection of all potential cone-opponent neurons (see **Methods**). Second, data was collected from a single imaging plane for each macaque and somas within the foveal ganglion cell layer are coarsely stratified (Perry and Silveira, 1988). For example, ON and OFF somas are generally found in different layers and rarer non-midget RGCs are found closest to the inner retina. Because our imaging area intersects the foveal slope which begins as a monolayer and gradually increases to 6 cells deep, neurons from all areas within the ganglion cell layer are imaged. As a result, sampling biases are mitigated, but not fully prevented.

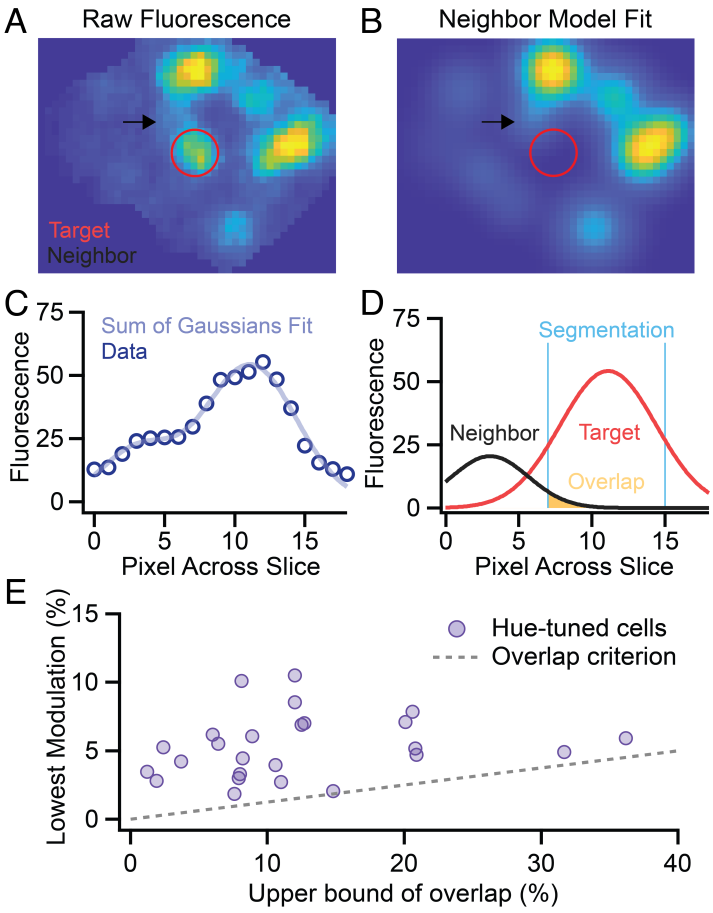

Figure 4. Sum of Gaussians model to verify optical isolation. (A) Fluorescence image of the neighborhood around a non-cardinal color cell (red). We chose this cell for demonstration due to the proximity of a neighbor cell (black arrow) and it is not representative of all non-cardinal color cells which typically have much less overlap. **(B)** The model fits a 2D Gaussian to each cell and the overlap is calculated from the area of neighboring cells within the target cell's segmentation mask. The result is an upper bound on overlap because the 2D Gaussian fit overestimates the cell's spatial footprint and the overlap from all neighboring cells was summed together. For display of overlap, the Gaussian representing the target cell is omitted. **(C, D)** A one-dimensional view of the fitting procedure and overlap calculation for the target cell and its nearest neighbor. **(E)** Comparison of the lowest modulation depth obtained across stimuli to the percent overlap from other cells within the target cell's segmentation mask. The maximum modulation explainable by crosstalk was bounded by the product of the percent overlap and the largest modulation observed across experiments (gray dashed line).

Confirming the optical isolation of neurons with non-cardinal responses.
A common concern with functional imaging is the possibility of response contamination from nearby cells. Could the neurons identified with L vs. M ± S opponency reflect the responses of two overlapping neurons, one with L vs.

M opponency and one with S-cone input? Here we manually segmented only cells that were laterally well-isolated across all imaging sessions, as previously described (Godat et al., 2022). Any out-of-focus cell eluding detection during segmentation would be very dim and expected to contribute weakly to a segmented cell's response. Our stringent responsivity criterion was chosen to eliminate such weak responses. Less than half of all visible cells in each region imaged met our criteria for segmentation and analysis. While these approaches have been successful in our past work, we sought to develop an additional method for quantitative verification of optical isolation.

We quantified optical isolation with a sum of Gaussians model for each non-cardinal color cell and its nearest neighbors (**Fig. 4**; see **Methods**). The model estimates an upper bound on the amount of fluorescence within each cell's segmentation mask that could have originated from neighboring cells. We fit each non-cardinal color cell and their nearest neighbors with two-dimensional Gaussians (**Fig. 4A-C**), then calculated the total overlap from all neighboring cells within the target cell's segmentation mask (**Fig. 4D**). The overlap was compared to the modulation depth of each non-cardinal color cell's weakest response to the cone-isolating stimuli (**Fig. 4E**). The maximum response that could be explained by crosstalk was determined as the product of the percent overlap and the largest modulation depth recorded across all neurons in the dataset (dashed line in **Fig. 4E**). The response amplitudes for all 25 L vs. M ± S neurons exceeded this threshold, indicating that their responses cannot be explained by crosstalk from nearby cells.

This model defines a highly stringent criterion that overestimates crosstalk in several ways. First, fitting somas with a two-dimensional Gaussian ignores the sharper borders of each cell and overestimates the spatial extent of each cell's light distribution, thus providing a generous estimate of the amount of overlap between cells that might have occurred. Second, the overlap percentage for each cell reflects the summed contributions of all neighboring cells. The stimulus responses of each neighboring cell were not considered as many were not segmented due to insufficient optical isolation (e.g., the neurons in the top right corner of **Fig. 4A**). Many neighboring cells could have been omitted based on their response properties (e.g., a neighbor that did not respond to the S-cone isolating stimulus is unlikely to contribute to the target cell's S-cone response), which would have reduced the summed overlap percentages plotted in **Fig. 4E**. However, because all 25 L vs. M ± S cells passed our initial overly-conservative test, these factors were not considered further.

DISCUSSION

A complete account of cone opponency in the retinal output is critical for efforts to understand how neurons give rise to color perception. Here we confirmed that neurons with both L vs. M cone opponency and S-cone input are present in the primate fovea. While it remains to be determined how downstream neurons use the responses of retinal neurons tuned to non-cardinal color directions, our results confirm that cone-opponent signals in the retinal output are more diverse than suggested by textbook models of color vision.

While anatomical experiments will be necessary to confirm cell type, we predict the L vs. M+S and M vs. L+S neurons are subtypes of midget RGCs, which are the only known L vs. M cone-opponent RGC type in primates. HI horizontal cell feedback is largely responsible for the L vs. M midget RGC's surround receptive field; however, feedback from S-cone-preferring HII horizontal cells has also been reported (Ahnelt and Kolb, 1994; Packer et al., 2010) and their input could contribute the S-cone response (Neitz and Neitz, 2017). The variable numbers of L- and M-cones in the surround receptive fields of L vs. M midget RGCs could explain both the L vs. M ± S neurons in **Fig. 3A** and the M+S and L+S neurons in **Fig. 3B**. Midget RGCs are the most common primate RGC type and are among the best-studied primate retinal neurons. However, there is precedent for unexpected cone opponency within the midget RGC population: S-OFF midget RGCs were once highly controversial but are now thought to make up 5% of all midget RGCs (Klug et al., 2003; Patterson et al., 2019). The absence of both S-OFF midget and L vs. M ± S RGCs from some prior surveys is likely due to their relatively low density. Eccentricity may also be an important factor. Our study was performed in the center of the fovea, a highly-specialized region largely inaccessible with standard retinal physiology techniques.

Our findings are consistent with a growing appreciation for the importance of rarer RGC types (Masland and Martin, 2007; Gollisch and Meister, 2010) and the capacity for retinal circuits to perform computations typically attributed to the cortex (Patterson et al., 2022). While the neurons tuned to non-cardinal color directions were relatively rare, their density alone does not rule out a potential contribution to color vision as they exceed the 2-3% density reported for foveal small bistratified RGCs (Dacey, 1993). In our dataset, the two groups with S-cone

ON input, (L+S)-M and (M+S)-L, were more common than those with S-cone OFF input. This imbalance could reflect intrinsic differences in the relative densities or experimental factors, such as the location of the imaging plane within the ganglion cell layer. Comparable numbers of L vs. M+S and M vs. L+S neurons have been reported in the retina (De Monasterio et al., 1975), while in the LGN, only the M-(L+S) group was lower (Tailby et al., 2008b). In the primary visual cortex where both contrast adaptation and non-cardinal cone opponency are more prevalent, L vs. M+S neurons are more common than M vs. L+S (Tailby et al., 2008a; Horwitz, 2020). Given their low density, a larger sample size will be necessary to confidently resolve and interpret the prevalence of each subtype.

The cardinal directions and their cone inputs have become standard features of color vision models (**Fig. 1C**). A second stage consisting of three independent orthogonal axes was appealing in its simplicity and agreement with the redundancy reduction hypothesis, a highly influential theory of neural coding at the time (Barlow, 1961). The cone inputs to the cardinal directions are sufficient and near optimal for efficiently encoding the variance present in the L-, M- and S-cone outputs (Buchsbaum and Gottschalk, 1983; Atick et al., 1992, 1993). This hypothesis predicts additional forms of cone opponency are unnecessary because they overlap with the cardinal directions and thus carry redundant spectral information.

However, evidence for greater diversity was present even in the initial work establishing the cardinal directions in the form of residual selectivity for intermediate color directions (Krauskopf et al., 1982) and in the rare LGN neurons with both L vs. M opponency and S-cone input (Derrington et al., 1984). A reanalysis of the psychophysical data revealed evidence for additional "higher order" mechanisms tuned to intermediate color directions (Krauskopf et al., 1986). Subsequent psychophysics provided additional support for higher-order mechanisms and questioned the independence of the cardinal mechanisms (Krauskopf et al., 1986; Krauskopf and Farell, 1990; Webster and Mollon, 1991, 1994; Zaidi and Halevy, 1993; Li and Lennie, 1997; Danilova and Mollon, 2012b, 2012a). As the name "higher-order mechanism" suggests, the non-cardinal color tuning is assumed to arise in the cortex (third stage in **Fig. 1C**) (De Valois and De Valois, 1993; Zaidi and Shapiro, 1993). However, our results indicate that some non-cardinal color tuning begins in the retina, earlier in the visual system than classically thought.

Despite the growing consensus that the cardinal directions alone cannot fully account for color perception, the salience of the L vs. M and S vs. L+M color directions has strong support [reviewed in (Eskew, 2009; Stockman and Brainard, 2010)]. Consistent with previous physiological surveys (De Monasterio and Gouras, 1975; Derrington et al., 1984; Sun et al., 2006; Tailby et al., 2008b), most neurons in **Fig. 3A** fell along the cardinal axes. The numerical dominance of these neurons in the retinal output could provide a simple explanation for the superior detection L vs. M and S vs. L+M stimuli. While weak S-cone input to the L vs. M mechanism has been reported in some threshold experiments measuring color detection (Stromeyer et al., 1998), the strongest support for non-cardinal color mechanisms comes from suprathreshold experiments that measure color appearance. A key feature of the multi-stage color vision models (**Fig. 1C**) is that the results of both psychophysical paradigms are accounted for. Both color detection and color appearance are important aspects of human color vision requiring explanation at the level of neural circuitry. The L vs. M+S and M vs. L+S neurons identified here open new avenues of research for modeling the neural circuits contributing to human color vision. Given the lack of contrast adaptation measured in cone-opponent RGCs and their LGN projections (Solomon et al., 2004; Tailby et al., 2008a, 2008b), retinal circuitry likely provides the beginnings of an explanation rather than the final answer.

While comparative psychophysics supports macaques as a model of human color vision (De Valois et al., 1974; Stoughton et al., 2012; Gagin et al., 2014; Horwitz, 2015; Gelfand and Horwitz, 2018), the possibility of species differences between macaque and human color vision was raised by a recent comparative anatomy study (Kim et al., 2023). Retinal circuits that mix L/M- and S-cones and could create L vs. M $\pm$ S opponency were reported in a human retina, but not in a macaque retina. Determining the functional impact of the human-specific circuits is a vital next step and is possible with recent advances in human retinal physiology (Soto et al., 2020; Reinhard and Münch, 2021; Shah et al., 2021). The next steps for macaque physiology include determining how the response properties of L vs. M $\pm$ S neurons vary with the spatiotemporal stimulus properties and different adaptation states. Importantly, the recent discussion on species differences emphasizes how the most common macaque RGCs differ from human color appearance but overlooks their similarities to human color detection; both aspects require explanation at the level of the early visual system.

Despite centuries of study, the underlying mechanisms of color vision remain an unsolved mystery and even foundational hypotheses in color vision are debated (Pugh and Kirk, 1986; Gegenfurtner and Hawken, 1996; Es-

kew, 2009; Kamar et al., 2019; Conway et al., 2023). The confirmation of L vs. M ± S neurons in the primate retina indicates that models assuming cone opponency in the early visual system is limited to just two cardinal mechanisms may be worth revisiting as they may not take advantage of the full diversity of cone-opponent information in the retinal output. Higher-order mechanisms were initially proposed as labelled lines for color (Krauskopf et al., 1986) and it has been said that, from a computational perspective, that they make little sense otherwise (Eskew, 2009). Indeed, models where the second stage consists of L vs. M+S and M vs. L+S neurons can account for many aspects of color perception (Schmidt et al., 2014, 2016; Rezeanu et al., 2023). Furthermore, models examining the interaction between cardinal and non-cardinal mechanisms remain unexplored and could be a productive avenue for future research. Some studies indicate that six L vs. M mechanisms are necessary to fully account for color detection (Shepard et al., 2017). These six mechanisms would correspond the six L vs. M cone-opponent groups identified here (L-M, M-L, LS-M, MS-L, L-MS and M-LS) as these are the only possible L vs. M combinations. Ultimately, a comprehensive account of the neural mechanisms of color perception will require consideration of all cone-opponent neurons, including those tuned to non-cardinal color directions.

ACKNOWLEDGEMENTS

We thank Amber Walker for animal anesthesia during imaging, David Brainard and Jay Neitz for valuable discussions, the vector core at the Perelman School of Medicine of the University of Pennsylvania, the Genetically-Encoded Neuronal Indicator and Effector (GENIE) project, and the Janelia Research Campus of the Howard Hughes Medical Institute. This work was supported by NIH grants F32-EY032318 (SSP), K99-EY035323 (SSP), P30-EY00131944, R01-EY021166 (WHM), R01-EY031467 (DRW), T32-EY007125 (TG, SSP) and U01-EY025467, Air Force Office of Scientific Research grants FA-9550-22-1-0044 (DRW) and FA-9550-22-1-0167 (DRW), and Research to Prevent Blindness through an unrestricted grant to the Flaum Eye Institute.

DECLARATION OF INTERESTS

DRW has patents with the University of Rochester (#6199986, #6264328, and #6338559) and has consulted for Warby Parker. QY has patents with the University of Rochester, Canon Inc., and the University of Montana (#9226656, #9406133, and #9454084) and has consulted for Oculus VR and Boston Micromachine Corporation. SSP has a patent application filed with the University of Washington (#17/612061).

AUTHOR CONTRIBUTIONS

TG, JEM, WHM, DRW and SSP conceived of the project and designed experiments; TG and JEM collected the data; TG, KK, JEM and SSP analyzed the calcium imaging data; TG and SSP created the figures; KP and QY provided software and hardware; TG and SSP wrote the paper with input from DRW.

REFERENCES

1. Ahnelt PK, Kolb H (1994) Horizontal cells and cone photoreceptors in human retina: A Golgi-electron microscope study of spectral connectivity. *J Comp Neurol* 343:406–427.
2. Atick JJ, Li Z, Redlich AN (1992) Understanding retinal color coding from first principles. *Neural Comput* 4:559–572.
3. Atick JJ, Li Z, Redlich AN (1993) What does post-adaptation color appearance reveal about cortical color representation? *Vision Res* 33:123–129.
4. Barlow H (1961) Possible principles underlying the transformations of sensory messages. In: Sensory Communication (Rosenbith WA, ed), pp 217–234. Cambridge, MA: MIT Press.
5. Baron WS (1973) Maxwellian View stimulator for electrophysiological or psychophysical work. *Appl Opt* 12:2560–2562.
6. Baudin J, Angueyra JM, Sinha R, Rieke F (2019) S-cone photoreceptors in the primate retina are functionally distinct from L and M cones. *Elife* 8:1–22.
7. Boynton RM, Kambe N (1980) Chromatic difference steps of moderate size measured along theoretically critical axes.*Color Res Appl* 5:13–23.
8. Brainard DH (1996) Cone contrast and opponent modulation color spaces. In: Human Color Vision (Kaiser PK, Boynton RM, eds), pp 563–579. Washington, DC: Optical Society of America.
9. Brainard DH (1997) The Psychophysics Toolbox. *Spat Vis* 10:433–436.
10. Buchsbaum G, Gottschalk A (1983) Trichromacy, opponent colours coding and optimum colour information in the retina. *Proc R Soc London Ser B* 220:89–113.
11. Buzás P, Blessing EM, Szmajda BA, Martin PR (2006) Specificity of M and L cone inputs to receptive fields in the parvocellular pathway: Random wiring with functional bias. *J Neurosci* 26:11148–11161.
12. Calkins DJ (2000) Representation of cone signals in the primate retina. *J Opt Soc Am A* 17:597–606.
13. Calkins DJ, Sterling P (1996) Absence of spectrally specific lateral inputs to midget ganglion cells in primate retina. *Nature* 381:613–615.
14. Calkins DJ, Sterling P (1999) Evidence that circuits for spatial and color vision segregate at the first retinal synapse. *Neuron* 24:313–321.
15. Chatterjee S, Callaway EM (2003) Parallel colour-opponent pathways to primary visual cortex. *Nature* 426:668–671.
16. Chen TW, Wardill TJ, Sun Y, Pulver SR, Renninger SL, Baohan A, Schreiter ER, Kerr RA, Orger MB, Jayaraman V, Looger LL, Svoboda K, Kim DS (2013) Ultrasensitive fluorescent proteins for imaging neuronal activity. *Nature* 499:295–300.
17. Conway BR (2001) Spatial structure of cone inputs to color cells in alert macaque primary visual cortex (V-1). *J Neurosci* 21:2768–2783.
18. Conway BR, Malik-Moraleda S, Gibson E (2023) Color appearance and the end of Hering's Opponent-Colors Theory. *Trends Cogn* Sci:1–14.
19. Curcio CA, Allen KA (1990) Topography of ganglion cells in human retina. *J Comp Neurol* 300:5–25.
20. Dacey DM (1993) Morphology of a small-field bistratified ganglion cell type in the macaque and human retina. *Vis Neurosci* 10:1080–1098.
21. Dacey DM, Packer OS (2003) Colour coding in the primate retina: diverse cell types and cone-specific circuitry. *Curr Opin Neurobiol* 13:421–427.
22. Danilova M V., Mollon JD (2012a) Cardinal axes are not independent in color discrimination. *J Opt Soc Am A* 29:A157.
23. Danilova M V, Mollon JD (2012b) Foveal color perception: minimal thresholds at a boundary between perceptual categories. *Vision Res* 62:162–172.
24. De Monasterio FM (1978) Signals from blue cones in "red-green" opponent-color ganglion cells of the macaque retina. *Vision Res* 19:441–449.
25. De Monasterio FM, Gouras P (1975) Functional properties of ganglion cells of the rhesus monkey retina. *J Physiol* 251:167–195.
26. De Monasterio FM, Gouras P, Tolhurst DJ (1975) Trichromatic colour opponency in ganglion cells of the rhesus monkey retina. *J Physiol* 251:197–216.

27. De Valois RL, Morgan HC, Polson MC, Mead WR, Hull EM (1974) Psychophysical studies of monkey vision. I. Macaque luminosity and color vision tests. *Vision Res* 14:53–67
28. De Valois RL (2004a) The neural coding of color. In: The New Visual Neurosciences (Werner JS, Chalupa LM, eds), pp 1003–1013. MIT Press.
29. De Valois RL, De Valois KK (1993) A multi-stage color model. *Vision Res* 33:1053–1065.
30. Derrington AM, Krauskopf J, Lennie P (1984) Chromatic mechanisms in lateral geniculate nucleus of macaque. *J Physiol* 357:241–265.
31. Derrington AM, Lennie P (1984) Spatial and temporal contrast sensitivities of neurones in lateral geniculate nucleus of macaque. *J Physiol* 357:219–240..
32. Eskew RT (2009) Higher order color mechanisms: A critical review. *Vision Res* 49:2686–2704.
33. Field GD, Gauthier JL, Sher A, Greschner M, Machado TA, Jepson LH, Shlens J, Gunning DE, Mathieson K, Dabrowski W, Paninski L, Litke AM, Chichilnisky EJ (2010) Functional connectivity in the retina at the resolution of photoreceptors. *Nature* 467:673–677.
34. Fuld K, Wooten BR, Whalen JJ (1981) The elemental hues of short-wave and extraspectral lights. *Percept Psychophys* 29:317–322.
35. Gagin G, Bohon KS, Butensky A, Gates MA, Hu JY, Lafer-Sousa R, Pulumo RL, Qu J, Stoughton CM, Swanbeck SN, Conway BR (2014) Color-detection thresholds in rhesus macaque monkeys and humans. *J Vis* 14:1–15.
36. Gegenfurtner KR, Hawken MJ (1996) Interaction of motion and color in the visual pathways. *Trends Neurosci* 19:394–401.
37. Gelfand EC, Horwitz GD (2018) Model of parafoveal chromatic and luminance temporal contrast sensitivity of humans and monkeys. *J Vis* 18:1–17.
38. Godat T, Cottaris NP, Patterson S, Kohout K, Parkins K, Yang Q, Strazzeri JM, McGregor JE, Brainard DH, Merigan WH, Williams DR (2022) In vivo chromatic and spatial tuning of foveolar retinal ganglion cells in Macaca fascicularis. *PLoS ONE* 17:e0278261.
39. Gollisch T, Meister M (2010) Eye smarter than scientists believed: neural computations in circuits of the retina. *Neuron* 65:150–164.
40. Gray DC, Merigan W, Wolfing JI, Gee BP, Porter J, Dubra A, Twietmeyer TH, Ahmad K, Tumbar R, Reinholz F, Williams DR (2006) In vivo fluorescence imaging of primate retinal ganglion cells and retinal pigment epithelial cells. *Opt Express* 14:7144.
41. Horwitz GD (2015) What studies of macaque monkeys have told us about human color vision. *Neuroscience* 296:110–115.
42. Horwitz GD (2020) Signals related to color in the early visual cortex. *Annu Rev Vis Sci* 6:287–311.
43. Ingling CR (1977) The spectral sensitivity of the opponent-color channels. *Vision Res* 17:1083–1089.
44. Kamar S, Howlett MHC, Kamermans M (2019) Silent-substitution stimuli silence the light responses of cones but not their output. *J Vis* 19:1–11.
45. Kim YJ, Packer O, Pollreisz A, Martin PR, Grunert U, Dacey DM (2023) Comparative connectomics reveals noncanonical wiring for color vision in human foveal retina. *Proc Natl Acad Sci* 120:e2300545120.
46. Klug K, Herr S, Ngo IT, Sterling P, Schein S (2003) Macaque retina contains an S-cone OFF midget pathway. *J Neurosci* 23:9881–9887.
47. Krauskopf J, Farell B (1990) Influence of colour on the perception of motion. *Nature* 348:328–332.
48. Krauskopf J, Williams DR, Heeley DW (1982) Cardinal directions of color space. *Vision Res* 22:1123–1131.
49. Krauskopf J, Williams DR, Mandler MB, Brown AM (1986) Higher order color mechanisms. *Vision Res* 26:23–32.
50. Lee BB, Cooper B, Cao D (2018) The spatial structure of cone-opponent receptive fields in macaque retina. *Vision Res* 151:141–151.
51. Lennie P, D'Zmura M (1988) Mechanisms of color vision. *Crit Rev Neurobiol* 3:333–400.
52. Lennie P, Haake PW, Williams DR (1991) The design of chromatically opponent receptive fields. In: Computational Models of Visual Processing (Landy MS, Movshon JA, eds), pp 71–82. Cambridge, MA: MIT Press.
53. Li A, Lennie P (1997) Mechanisms underlying segmentation of colored textures. *Vision Res* 37:83–97.
54. Li P, Garg AK, Zhang LA, Rashid MS, Callaway EM (2022) Cone opponent functional domains in primary

visual cortex combine signals for color appearance mechanisms.*Nat Commun* 13.
55. Liang J, Williams DR (1997) Aberrations and retinal image quality of the normal human eye. *J Opt Soc Am A* 14:2873–2883.
56. Ma ICK, Nasir-Ahmad S, Lee SCS, Grünert U, Martin PR (2023) Contribution of parasol-magnocellular pathway ganglion cells to foveal retina in macaque monkey. *Vision Res* 202:108154.
57. Masland RH, Martin PR (2007) The unsolved mystery of vision. *Curr Biol* 17:577–582.
58. Mazzaferri MA, Yang E, Bordt AS, Patterson SS, Kuchenbecker JA, Neitz M, Neitz J (2023) The narrow thorny is an S-ON/S-OFF ganglion cell in the primate retina. *Investig Ophthalmol Vis Sci* 64:4381.
59. McGregor JE, Godat T, Dhakal KR, Parkins K, Strazzeri JM, Bateman BA, Fischer WS, Williams DR, Merigan WH (2020) Optogenetic restoration of retinal ganglion cell activity in the living primate.*Nat Commun* 11:1703.
60. McGregor JE, Yin L, Yang Q, Godat T, Huynh KT, Zhang J, Williams DR, Merigan WH (2018) Functional architecture of the foveola revealed in the living primate. *PLoS ONE* 13:e0207102.
61. Neitz J, Neitz M (2017) Evolution of the circuitry for conscious color vision in primates. *Eye* 31:286–300.
62. Packer OS, Verweij J, Li PH, Schnapf JL, Dacey DM (2010) Blue-yellow opponency in primate S-cone photoreceptors. *J Neurosci* 30:568–572.
63. Padmos P, Norren D V. (1975) Cone systems interaction in single neurons of the lateral geniculate nucleus of the macaque. *Vision Res* 15:617–619.
64. Patterson SS, Bembry BN, Mazzaferri MA, Neitz M, Rieke F, Soetedjo R, Neitz J (2022) Conserved circuits for direction selectivity in the primate retina. *Curr Biol* 32:2529–2538.
65. Patterson SS, Kuchenbecker JA, Anderson JR, Bordt AS, Marshak DW, Neitz M, Neitz J (2019) An S-cone circuit for edge detection in the primate retina. *Sci Rep* 9:11913.
66. Patterson SS, Kuchenbecker JA, Anderson JR, Neitz M, Neitz J (2020a) A color vision circuit for non-image-forming vision in the primate retina. *Curr Biol* 30:1269–1274.
67. Patterson SS, Mazzaferri MA, Bordt AS, Chang J, Neitz M, Neitz J (2020b) Another Blue-ON ganglion cell in the primate retina. *Curr Biol* 30:R1409–R1410.
68. Perry VH, Silveira LCL (1988) Functional lamination in the ganglion cell layer of the macaque's retina. *Neuroscience* 25:217–233.
69. Pugh EN, Kirk DB (1986) The pi mechanisms of W S Stiles: an historical review. *Perception* 15:705–728.
70. Reinhard K, Münch TA (2021) Visual properties of human retinal ganglion cells. *PLoS ONE* 16:e0246952.
71. Rezeanu D, Neitz M, Neitz J (2023) From cones to color vision: a neurobiological model that explains the unique hues. *J Opt Soc Am A* 40:A1–A8.
72. Rodieck R (1991) Which cells code for color? In: From Pigments to Perception: Advances in Understanding Visual Processes (Valberg A, Lee B, eds), pp 83–93. London: Plenum Press.
73. Sankeralli MJ, Mullen KT (1997) Postreceptoral chromatic detection mechanisms revealed by noise masking in three-dimensional cone contrast space. *J Opt Soc Am A* 14:2633–2646.
74. Schmidt BP, Neitz M, Neitz J (2014) Neurobiological hypothesis of color appearance and hue perception. *J Opt Soc Am A* 31:195–207.
75. Schmidt BP, Touch P, Neitz M, Neitz J (2016) Circuitry to explain how the relative number of L and M cones shapes color experience. *J Vis* 16:1–17.
76. Shah NP, Brackbill N, Samarakoon R, Rhoades C, Kling A, Sher A, Litke A, Singer Y, Shlens J, Chichilnisky EJ (2021) Individual variability of neural computations in the primate retina. *Neuron* 110:698-708.e5.
77. Shepard TG, Lahlaf SI, Eskew RT (2017) Labeling the lines: A test of a six-mechanism model of chromatic detection. *J Vis* 17:1–18.
78. Shevell SK, Martin PR (2017) Color opponency: tutorial. *J Opt Soc Am A* 34:1099–1108.
79. Sinha R, Hoon M, Baudin J, Okawa H, Wong ROL, Rieke F (2017) Cellular and circuit mechanisms shaping the perceptual properties of the primate fovea. *Cell* 168:413–426.
80. Solomon SG, Peirce JW, Dhruv NT, Lennie P (2004) Profound contrast adaptation early in the visual pathway. *Neuron* 42:155–162.
81. Soto F, Hsiang JC, Rajagopal R, Piggott K, Harocopos GJ, Couch SM, Custer P, Morgan JL, Kerschensteiner D (2020) Efficient coding by midget and parasol ganglion cells in the human retina. *Neuron*:1–11.
82. Stockman A, Brainard DH (2010) Color vision mechanisms. Opt Soc Am Handb Opt:11.1–11.104.

83. Stoughton CM, Lafer-Sousa R, Gagin G, Conway BR (2012) Psychophysical chromatic mechanisms in macaque monkey. *J Neurosci* 32:15216–15226.
84. Stromeyer CF, Chaparro A, Rodriguez C, Chen D, Hu E, Kronauer RE (1998) Short-wave cone signal in the red-green detection mechanism. *Vision Res* 38:813–826.
85. Sun H, Smithson HE, Zaidi Q, Lee BB (2006) Specificity of cone inputs to macaque retinal ganglion cells. *J Neurophysiol* 95:837–849.
86. Tailby C, Solomon SG, Dhruv NT, Lennie P (2008a) Habituation reveals fundamental chromatic mechanisms in striate cortex of macaque. *J Neurosci* 28:1131–1139.
87. Tailby C, Solomon SG, Lennie P (2008b) Functional asymmetries in visual pathways carrying S-cone signals in macaque. *J Neurosci* 28:4078–4087.
88. Webster MA, Miyahara E, Malkoc G, Raker VE (2000a) Variations in normal color vision. I. Cone-opponent axes. *J Opt Soc Am A* 17:1535–1544.
89. Webster MA, Miyahara E, Malkoc G, Raker VE (2000b) Variations in normal color vision. II. Unique hues. *J Opt Soc Am A* 17:1535–1544.
90. Webster MA, Mollon JD (1991) Changes in colour appearance following post-receptoral adaptation. *Nature* 353:737–740.
91. Webster MA, Mollon JD (1994) The influence of contrast adaptation on color appearance. *Vision Res* 34:1993–2020.
92. Werner JS, Wooten BR (1979) Opponent chromatic mechanisms: Relation to photopigments and hue naming. *J Opt Soc Am* 69:422–434.
93. Westheimer G (1966) The Maxwellian view. *Vision Res* 6:669–682.
94. Williams DR, Burns SA, Miller DT, Roorda A (2023) Evolution of adaptive optics retinal imaging [Invited]. *Biomed Opt Express* 14:1307–1338.
95. Yang Q, Zhang J, Nozato K, Saito K, Williams DR, Roorda A, Rossi EA (2014) Closed-loop optical stabilization and digital image registration in adaptive optics scanning light ophthalmoscopy. *Biomed Opt Express* 5:3174–3191.
96. Yin L, Greenberg K, Hunter JJ, Dalkara D, Kolstad KD, Masella BD, Wolfe R, Visel M, Stone D, Libby RT, DiLoreto D, Schaffer D, Flannery J, Williams DR, Merigan WH (2011) Intravitreal injection of AAV2 transduces macaque inner retina. *Investig Ophthalmol Vis Sci* 52:2775–2783.
97. Yin L, Masella B, Dalkara D, Zhang J, Flannery JG, Schaffer D V., Williams DR, Merigan WH (2014) Imaging light responses of foveal ganglion cells in the living macaque eye. *J Neurosci* 34:6596–6605.
98. Zaidi Q, Halevy D (1993) Visual mechanisms of color changes. *Vision Res* 33:1037–1051.
99. Zaidi Q, Shapiro AG (1993) Adaptive orthogonalization of opponent-color signals. *Biol Cybern* 69:415–428.